Journal of Energy Storage 91 (2024) 112039

Contents lists available at ScienceDirect

Journal of Energy Storage

journal homepage: www.elsevier.com/locate/est

Research papers

Rose-like Ni-Co-Mn-S@N-CDs electrode material for flexible hybrid supercapacitors with high electrochemical performance

Bin Lu [a], Guo-Tao Xiang [a], Jia-Lei Xu [a], Rui-Dong Shi [a], Na Chen [a], Yong-Da Hu [b,*], Raul D. Rodriguez [c], Jin-Ju Chen [a,*]

[a] School of Materials and Energy, University of Electronic Science and Technology of China, Chengdu 610054, PR China
[b] School of Integrated Circuit Science and Engineering, University of Electronic Science and Technology of China, Chengdu 610054, PR China
[c] Research School of Chemistry & Applied Biomedical Sciences, Tomsk Polytechnic University, Lenina Ave. 30, 634050 Tomsk, Russia

ARTICLE INFO

Keywords:
Hybrid supercapacitor
Specific capacitance
Cycling stability
Structural design

ABSTRACT

Ternary transition metal sulfides are extensively considered as supercapacitor electrode materials due to their remarkable electrochemical properties. However, inferior electrical conductivity and structural stability severely limit their applications. Here, we address these limitations by introducing N-doped carbon dots (N-CDs) into Ni-Co-Mn-S nanoflowers via a two-step hydrothermal process followed by electrodeposition. Ni-Co-Mn-S nanoflowers feature a skeleton structure supporting rich ion transfer paths and abundant active sites, while electrodeposited N-CDs increase the electrical conductivity and enhance the cycling performance. The resulting Ni-Co-Mn-S@N-CDs material demonstrates a remarkable specific capacity of 2267 F g^{-1} at 1 A g^{-1} and maintains 96.2 % capacity after 10,000 cycles at 10 A g^{-1}. Moreover, this electrode material allows the development of hybrid supercapacitors with an impressive energy density of 61.6 Wh kg^{-1} at 800 W kg^{-1} and a superior capacitance retention of 89.0 % after 20,000 charge/discharge cycles at 5 A g^{-1}, alongside an excellent flexibility under various deformations. These findings represent a significant advancement in hybrid solid-state supercapacitors with promising implications for flexible energy storage technologies.

1. Introduction

Renewable energy sources, such as photovoltaic, wind, and hydropower, have been extensively developed to deal with the energy crisis and environmental pollution arising from the massive consumption of fossil energy sources [1]. Given the inherent limitations of these energy sources being easily influenced by the climate and geography, reliable energy storage becomes essential. Consequently, developing efficient and long-lasting energy storage devices is a research priority worldwide. Supercapacitors have superior power density than traditional batteries and better energy density than traditional capacitors, making them a hot research topic in recent years [2]. These devices, due to their high capacity, extended cycle life, rapid charging and discharging rate, and wide applicable temperature range are increasingly integrated into daily life applications [3]. For instance, supercapacitors play a critical role in starting and energy recovery systems of electric vehicles, and in frequency regulation for wind and solar power generation systems. Additionally, they are found extensive use in smart water, electricity, and gas meters facilitating long-term maintenance-free operation [4]. Supercapacitors also serve as crucial backup power sources for electronic devices like smartphones and computers with storage functions [5]. In particular, hybrid supercapacitors have the characteristics of pseudocapacitance and double-layer capacitance, which rely on Faraday redox reactions and electrostatic adsorption effect, respectively [6]. These two energy storage features lead to a substantial enhancement in the electrochemical properties of supercapacitors. Meanwhile, the positive and negative electrodes of hybrid supercapacitors have distinct voltage windows, resulting in a broad operating voltage range and excellent energy density [7]. The demand for efficient and sustainable energy storage solutions increasing in the face of global energy challenges drives the need for innovative electrode materials with enhanced performance and stability.

Among different types of electrode materials, transition metal sulfides (TMSs) have higher conductivity than transition metal oxides and hydroxides [8]. Variable valence states of metal ions give TMSs high redox activity and theoretical specific capacity [9,10]. TMSs are

---

* Corresponding authors.
E-mail addresses: yongnet169@uestc.edu.cn (Y.-D. Hu), jinjuchen@uestc.edu.cn (J.-J. Chen).

https://doi.org/10.1016/j.est.2024.112039
Received 26 January 2024; Received in revised form 7 April 2024; Accepted 12 May 2024
Available online 20 May 2024

classified into two categories according to dimension. The M_xS_y (M = Ni, Co, Mn, Zn, Fe, etc.) material with a three-dimensional structure has higher electrical conductivity and more redox active sites than MS_2 (M = W, Mo) with a layered structure [11], and generally exhibits higher specific capacity. In particular, ternary metal sulfides have much higher redox activity than single or binary transition metal sulfides due to multi-element valence and cooperative interaction among metal sulfides [12,13]. Yan et al. [14] prepared NiCoMnS on nickel foam (NF) to form a self-supporting electrode with a three-dimensional honeycomb structure, which exhibited desirable electrochemical activity due to the benefits of complementary multi-component systems. Liu et al. [15] introduced Fe dopants into nickel-cobalt sulfide composites to obtain Fe-NiCo-S electrode materials for supercapacitors, showing good charge storage kinetics and activity.

However, the slow reaction rate and volume expansion in the charge and discharge process still set TMSs far from ideal specific capacity and cycle stability [16]. On the one hand, the structural design of materials allows rich ion/electron transport channels to increase redox activity. This effective strategy includes designing hollow rod-like structures [12], hierarchical structures [14], porous structures [17], and core-shell structures [18]. On the other hand, due to the high electrochemical stability and strong conductivity, carbon materials are often combined with TMSs to buffer the volume change during cycling and improve the rate performance by reducing ion transport obstruction [19,20]. For instance, porous hollow N-doped carbon dots/NiCoS [21], NiCo/C@$NiCoS_x$ core-shell structure [22], and CoS_2/$NiCo_2S_4$/RGO nanohybrids [23] were developed to improve capacitance retention.

Compared with 1D and 2D carbon materials, carbon dots (CDs) with a much smaller size are more easily accessible to TMSs as reinforcement materials to mitigate volume variation during the cycling process [24]. The interior of CDs is mainly composed of highly conductive sp^2 hybridized carbon, effectively increasing the charge transfer rate and improving the rate performance of supercapacitors [25]. Meanwhile, CDs are rich in hydrophilic functional groups, which introduces plentiful active sites for capacitance increase and enhances electrolyte ions penetrating into electrode materials to facilitate redox reactions [26]. In addition, the volume expansion of metal compounds can be alleviated by CDs during the cyclic process, thus boosting the stability of electrode materials [27]. Hydrothermal treatment is often used for combining CDs with transition metal materials. Although the cycling stability of composites prepared by this method has been improved [28,29], the morphology and properties of materials are usually difficult to control.

In this work, we have meticulously combined the structural design with CDs to create electrode materials for supercapacitors, where rose-like Ni-Co-Mn-S materials were obtained by a stepwise hydrothermal process followed by the introduction of N-doped carbon dots (N-CDs) using electrodeposition. Ni-Co-Mn-S nanoflowers composed of nanosheets have a skeleton structure supporting large ion/electron transfer paths and a high specific surface area providing plentiful redox active sites. Meanwhile, N-CDs reduce the electrical resistivity and increase the capacity retention of the composite material. The hybrid supercapacitor, featuring Ni-Co-Mn-S@N-CDs as the positive electrode, demonstrates impressive performance characteristics. It achieves an outstanding energy density of 61.6 Wh kg^{-1} at 800 W kg^{-1} and remarkable durability preserving 89.0 % capacity after 20,000 cycles at 5 A g^{-1}, demonstrating its robustness and long-term efficacy.

2. Experimental section

2.1. Materials

Glucose ($C_6H_{12}O_6$), metformin hydrochloride ($C_4H_{12}ClN_5$), urea ($(NH_2)_2CO$), nickel acetate tetrahydrate ($Ni(CH_3COO)_2·4H_2O$), cobalt acetate tetrahydrate ($Co(CH_3COO)_2·4H_2O$), manganese acetate tetrahydrate ($Mn(CH_3COO)_2·4H_2O$), ammonium fluoride (NH_4F), and sodium sulfide nonahydrate ($Na_2S·9H_2O$) were acquired from Macklin Reagent Co., Ltd. (Shanghai, China). Polyvinylidene fluoride (PVDF), polyvinyl alcohol (PVA), active carbon (AC), *N*-methyl-2-pyrrolidinone (NMP), acetylene black, and potassium hydroxide (KOH) were acquired from Aladdin Reagent Co., Ltd. (Shanghai, China). All the above chemical reagents are analytical grade without additional purification.

2.2. Preparation of N-CDs

We prepared N-CDs by using the hydrothermal method. Typically, 0.050 g of $C_6H_{12}O_6$ and 0.500 g of $C_4H_{12}ClN_5$ were dispersed in 50 mL of deionized water to form a mixed solution. The solution was then heated to 180 °C at 5 °C/min in a 100 mL Teflon-lined stainless steel reactor and kept for 4 h. The N-CDs were obtained by filtering the hydrothermal products through a 0.22 μm membrane and dialyzing them in deionized water for 24 h [30].

2.3. Preparation of electrode materials

Ni-Co-Mn-O/NF was prepared by hydrothermal method. Firstly, 0.373 g of $Ni(CH_3COO)_2·4H_2O$, 0.125 g of $Co(CH_3COO)_2·4H_2O$, 0.245 g of $Mn(CH_3COO)_2·4H_2O$, 0.148 g of NH_4F, and 0.600 g of $(NH_2)_2CO$ were dispersed in 70 mL of deionized water and stirred until completely dissolved. The obtained solution was diverted to a 100 mL Teflon-lined stainless steel reactor, and then a piece of NF (2 cm × 4 cm) was dipped into the solution. Ni-Co-Mn precursor on NF was prepared at 120 °C for 5 h. After drying at 60 °C for 12 h, the as-prepared sample was heated to 350 °C at 5 °C/min and held for 2 h to acquire the Ni-Co-Mn-O/NF.

A mixed solution was obtained by dispersing 2.08 g of $Na_2S·9H_2O$ in 60 mL of deionized water and stirring until completely dissolved. Then, the solution and the prepared Ni-Co-Mn-O/NF were put in a 100 mL Teflon-lined stainless steel reactor. Ni-Co-Mn-S/NF was obtained at 140 °C for 4 h after undergoing the sulfidation process. The mass of the Ni-Co-Mn-S sample loaded on the surface of NF is 5.2 mg.

Electrodeposition was carried out in a system using Ag/AgCl as the reference electrode, platinum plate as the counter electrode, and Ni-Co-Mn-S/NF as the working electrode. The electrolyte is consisting of 0.1 mg/mL N-CDs and 0.1 mol/L $(NH_4)_2SO_4$. Ni-Co-Mn-S@N-CDs/NF was prepared by the electrodeposition of N-CDs on Ni-Co-Mn-S at a constant voltage of −1 V for 3 min.

The assembly process of hybrid supercapacitors is described in the experimental section of the Supporting Information (SI).

2.4. Characterization

The morphologies and microstructures of samples were characterized by scanning electron microscopy (SEM, Ultra-55 Carl Zeiss, Germany) and transmission electron microscopy (TEM, FEI Tecnai G2, USA). The elemental composition and distribution information of materials were obtained by energy-dispersive X-ray spectroscopy (EDX, Aztec Live ULTIM, Oxford Instruments). Fourier transform infrared spectroscopy (FTIR, TENSOR 27, Bruker) was used to analyze the chemical bonding composition of the N-CDs sample. X-ray diffraction (XRD, D8-Advance, Bruker) with Cu Kα radiation was applied to study the phase and crystallinity of products. The elemental composition and chemical states of samples were evaluated using X-ray photoelectron spectroscopy (XPS, Thermo Scientific ESCALAB250Xi).

2.5. Electrochemical measurements

Electrochemical measurements were conducted on an electrochemical workstation (Chenhua CHI660E, Shanghai, China) by a conventional three-electrode system with 1.0 mol/L KOH as electrolyte. The reference, counter, and working electrodes are Hg/HgO, Pt sheet, and prepared samples, respectively. For the electrode samples involved in this experiment, we used cyclic voltammetry (CV), galvanostatic charge/discharge (GCD), and electrochemical impedance spectroscopy

(EIS) with Zview software to test and analyze the performance of these samples.

The specific capacitance (C_g, F g^{-1}) of electrodes and supercapacitors is evaluated using the following equation [31]:

$$C_g = \frac{I \bullet \Delta t}{m \bullet \Delta V} \tag{1}$$

where I (A) represents the current in the discharge process, Δt (s) represents the time of discharge, m (g) represents the mass of active materials, and ΔV (V) is the operating voltage. The power density (P, Wh kg^{-1}) and energy density (E, W kg^{-1}) of supercapacitors are evaluated as the following equations [32]:

$$E = \frac{0.5CV^2}{3.6} \tag{2}$$

$$P = \frac{3600E}{\Delta t} \tag{3}$$

where C (F g^{-1}) corresponds to the specific capacitance of supercapacitors, V (V) means the operating voltage, and Δt (s) represents the time of discharge.

3. Results and discussion

As shown in Fig. 1a, glucose and metformin hydrochloride molecules are uniformly heated in a hydrothermal reactor at 180 °C to synthesize N-CDs. The prepared N-CDs comprise carbon cores and passivation layers enriched with functional groups such as –OH and –NH_2, which can contribute to a large number of redox-active sites [21,30]. The preparation process of Ni-Co-Mn-S@N-CDs hybrids is shown in Fig. 1b. The hydrothermally synthesized Ni-Co-Mn precursor is dried and annealed to obtain the Ni-Co-Mn-O material, and then Ni-Co-Mn-S products are obtained by hydrothermal sulfuration. The rose-like Ni-Co-Mn-S@N-CDs hybrids are eventually obtained by electrodepositing N-CDs on the surface of Ni-Co-Mn-S material.

Fig. 2a and b displays the SEM images of Ni-Co-Mn-O materials, where a flower-like structure with flocculent edges is formed by interlaced growth of Ni-Co-Mn-O micrometer flakes. After sulfidation, the Ni-Co-Mn-S sample in Fig. 2c and d has a rose-shaped structure formed by intersecting flat hexagonal lamellae, which provides more active sites and smooth ions transport path for enhanced electrochemical performance, as well as providing the sample with a certain resistance to volume expansion and structural deformation during charging and discharging [33]. In Fig. 2e and f, after N-CDs electrodeposition on the surface of the Ni-Co-Mn-S sample, the obtained Ni-Co-Mn-S@N-CDs materials retain the stable rose-like structure. Fig. 2g and Fig. S1 in SI present the elemental composition and dispersion of the Ni-Co-Mn-S@N-CDs materials. The Ni, Co, Mn, S, C, N, and O elements distribution is consistent with the morphological image, confirming the successful composite between Ni-Co-Mn-S and N-CDs.

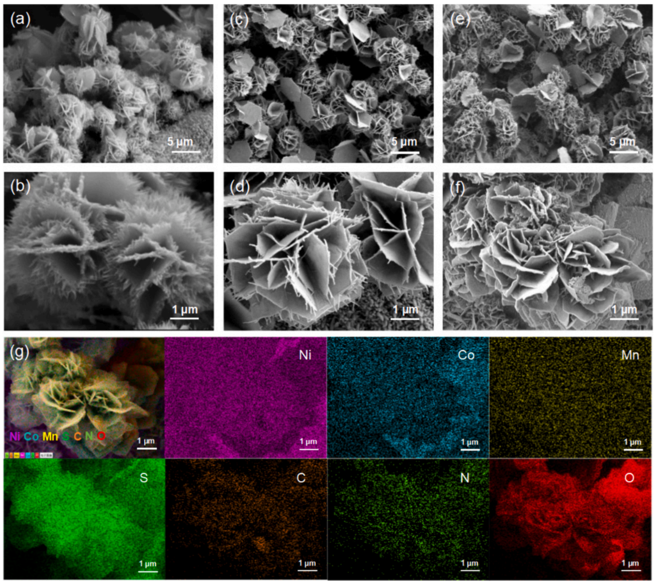

Fig. 2. SEM images of (a, b) Ni-Co-Mn-O, (c, d) Ni-Co-Mn-S, and (e, f) Ni-Co-Mn-S@N-CDs materials. (e) Elemental mapping images of the Ni-Co-Mn-S@N-CDs sample.

XRD and XPS measurements were conducted to investigate the crystalline structure, elemental composition, and chemical state of the Ni-Co-Mn-S@N-CDs sample. In the XRD spectrum of Fig. 3a, the characteristic peaks of the Ni-Co-Mn-S sample at 31.6°, 38.3°, 50.5°, and 55.3° are consistent with the (311), (400), (511), and (440) crystal planes of $NiCo_2S_4$ (JCPDS No. 20-0782), respectively, which indicates a cubic phase structure with the Fd3m space group [34]. Moreover, the characteristic peaks at 25.8°, 27.7°, 29.3°, and 49.9° correspond to the (100), (002), (101), and (103) crystal planes of the MnS with hexagonal phase (JCPDS No. 89-4089) [35]. The strong diffraction peaks occurring

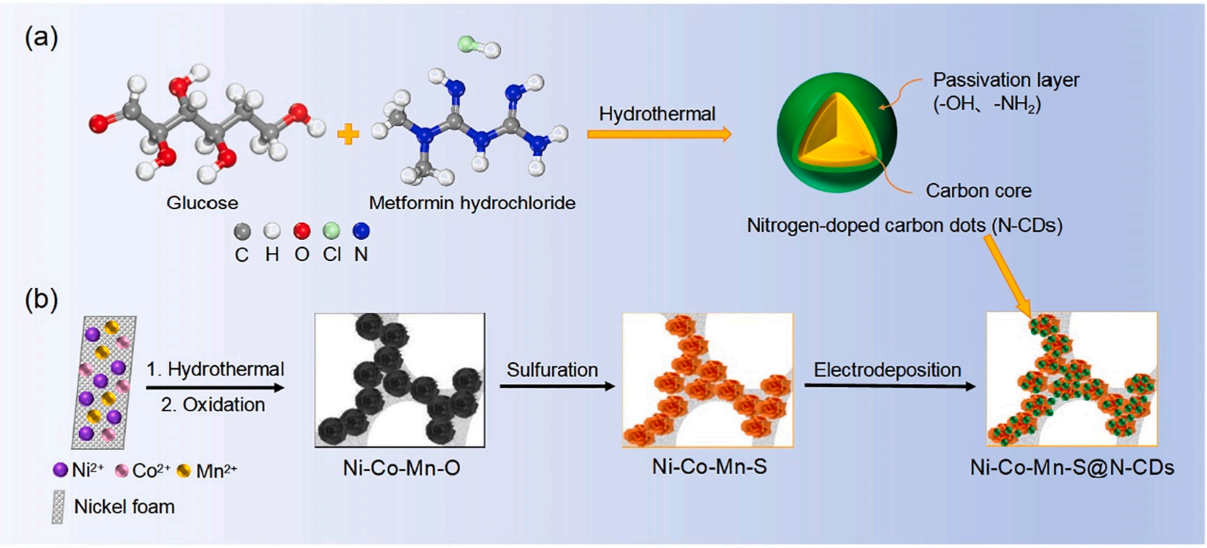

Fig. 1. Schematic illustration of the preparation process for (a) nitrogen-doped carbon dots (N-CDs) and (b) Ni-Co-Mn-S@N-CDs materials.

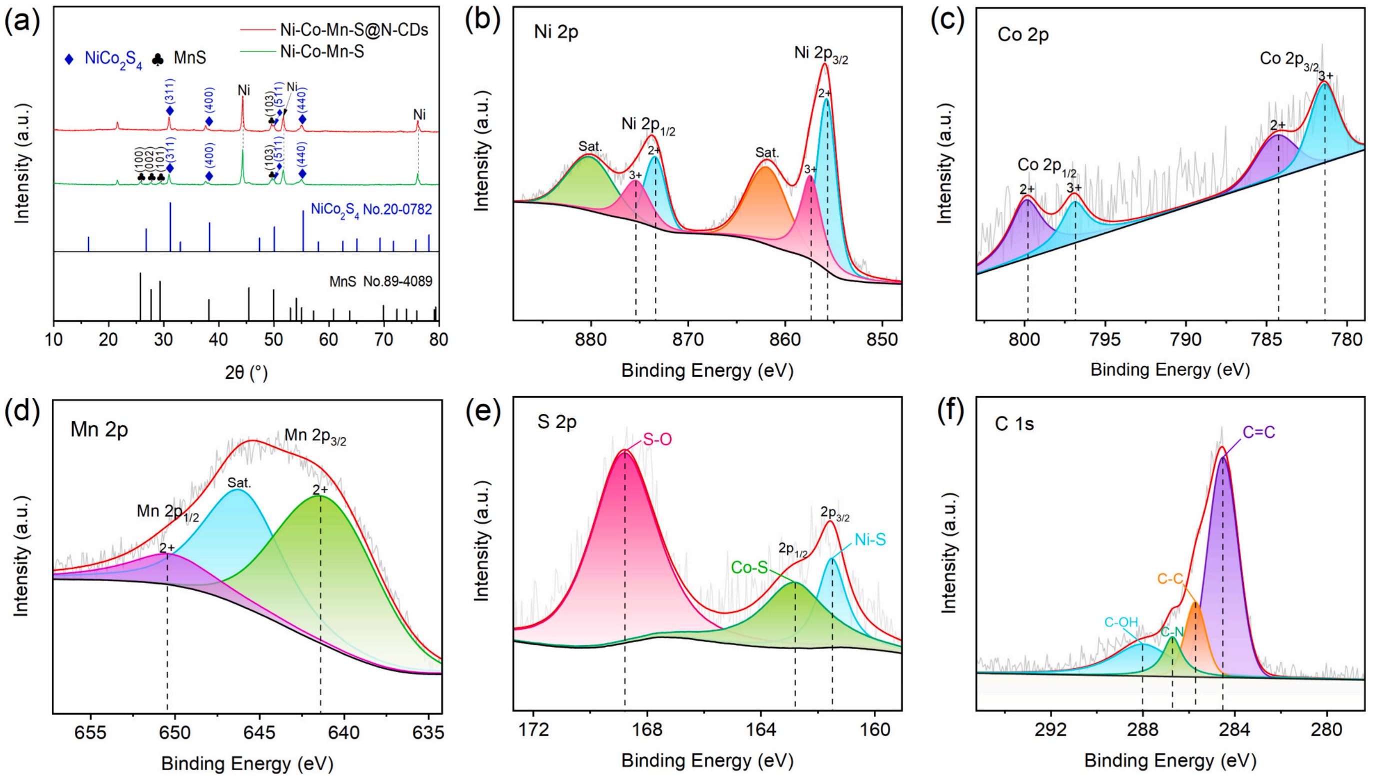

Fig. 3. (a) XRD patterns of Ni-Co-Mn-S and Ni-Co-Mn-S@N-CDs samples. High-resolution XPS spectra for (b) Ni 2p, (c) Co 2p, (d) Mn 2p, (e) S 2p, and (f) C 1s of the Ni-Co-Mn-S@N-CDs sample before charge/discharge cycle.

at 44.5°, 51.8°, and 76.2° come from NF. These results indicate that the Ni-Co-Mn-S sample is primarily comprised of $NiCo_2S_4$ and MnS. Compared with the Ni-Co-Mn-S sample, the XRD pattern of the Ni-Co-Mn-S@N-CDs sample shows no significant change, indicating that the N-CDs electrodeposition has almost no effect on the phase composition of the Ni-Co-Mn-S material. The distinctive peaks of N-CDs can hardly be found in the hybrid, which may be due to the low crystallinity of N-CDs.

The XPS survey spectrum of the Ni-Co-Mn-S@N-CDs sample is shown in Fig. S2 in SI, demonstrating the presence of Ni, Co, Mn, S, C and O elements in the material. Fig. 3b displays the XPS spectrum for Ni 2p of the Ni-Co-Mn-S@N-CDs sample, which exhibits two spin-orbital twin peaks of Ni $2p_{3/2}$ and Ni $2p_{1/2}$, as well as two satellite peaks. The spin energy difference between Ni $2p_{3/2}$ and Ni $2p_{1/2}$ calculated by spin-orbit coupling is approximately 17.9 eV, indicating the presence of both Ni^{3+} and Ni^{2+} in the Ni-Co-Mn-S@N-CDs. Specifically, the binding energies of Ni $2p_{3/2}$ at 857.4 eV and Ni $2p_{1/2}$ at 875.3 eV confirm the existence of Ni^{3+}, and the binding energies of Ni $2p_{3/2}$ at 855.6 eV and Ni $2p_{1/2}$ at 873.5 eV belong to Ni^{2+}. [16] For the Co 2p spectrum in Fig. 3c, peaks around 781.4 eV and 796.9 eV are related to Co^{3+}, and strong peaks around 784.4 eV and 799.9 eV can be attributed to Co^{2+} [33]. In addition, the spin energy difference between Co $2p_{1/2}$ and Co $2p_{3/2}$ calculated by spin-orbit coupling is about 15.5 eV, further confirming the existence of Co^{2+} and Co^{3+} in Ni-Co-Mn-S@N-CDs. In Fig. 3d, peaks of the Mn 2p spectrum at 641.0 eV and 650.4 eV belong to the spin-orbital of Mn $2p_{3/2}$ and Mn $2p_{1/2}$, respectively, which indicates the presence of Mn^{2+} [36]. Base on the XPS peak areas of elements Co and Mn, it can be evaluated that the molar ratio of $NiCo_2S_4$ and MnS in the Ni-Co-Mn-S@N-CDs sample is about 0.17:1. The S 2p spectrum is shown in Fig. 3f. Peaks at 162.9 eV and 161.5 eV belong to the S $2p_{1/2}$ and $2p_{3/2}$ of the metal sulfide, respectively [33]. The S—O bond originates from the inevitable surface oxidation and retention of oxidized components during synthesis. The XPS spectrum of C 1s is shown in Fig. 3f. The four peaks at 284.5 eV, 285.7 eV, 286.7 eV, and 288 eV are consistent with C═C, C—C, C—N, and C—OH bonds, respectively [37]. The strong C═C peak indicates a high number of carbon atoms in sp^2 hybridized form, which can enhance the electrochemical activity. The C—C bond confirms the existence of sp^3 hybridized carbon atoms. Moreover, the C—N and C—OH bonds demonstrate the abundant reactive functional groups on the surface of the N-CDs.

The TEM image of N-CDs in Fig. 4a demonstrates nearly spherical nanoparticles. Thanks to the hydrothermal method, the glucose molecules are sufficiently carbonized at a high temperature to obtain the “carbon core” of N-CDs [30]. The size distribution of N-CDs in Fig. 4b covers a range from 2 nm to 14 nm, with an average size of 7.88 nm. The FTIR pattern of N-CDs can be seen in Fig. 4c. The —OH groups that appear at 3235–3350 cm^{-1} and 1016 cm^{-1} are from the carbonized glucose [30]. The peaks at 1764 cm^{-1} and 1714 cm^{-1} belong to the C═O stretching vibration of the aldehyde group from glucose. Stretching vibrations C—C at 1200 cm^{-1} and C—H at 2935 cm^{-1} are due to the carbon skeleton of N-CDs core and $—CH_2$ of glucose, respectively [38]. C═N and C—N show characteristic peaks at 1616 cm^{-1} and 1413 cm^{-1}, which are from the metformin hydrochloride [39]. The results of the FTIR analysis suggest that the N-CDs are functionalized by a shell made up of —OH and nitrogenous groups, providing more active sites for enhancing capacitive performance.

Fig. 4d exhibits the TEM image of the sample Ni-Co-Mn-S@N-CDs, revealing a flower-like structure with a particle size of 4–5 μm in agreement with the SEM images (Fig. 3e and f). The lattice fringes of 0.283 nm and 0.247 nm in high-resolution TEM image of Fig. 4e are related to the (311) and (400) planes of cubic $NiCo_2S_4$, respectively [34]. Meanwhile, the lattice fringes of 0.304 nm and 0.182 nm are associated with the (101) and (103) planes of hexagonal MnS [35]. These analyses are compatible with the XRD results. In Fig. 4f, the selected area electron diffraction pattern further suggests the crystal composition of the Ni-Co-Mn-S@N-CDs material. The diffraction rings (yellow lines) can be classified as the crystal planes (311) and (400) of cubic $NiCo_2S_4$, and additional diffraction rings (white lines) are identified as the (101) and (201) crystal planes of hexagonal MnS.

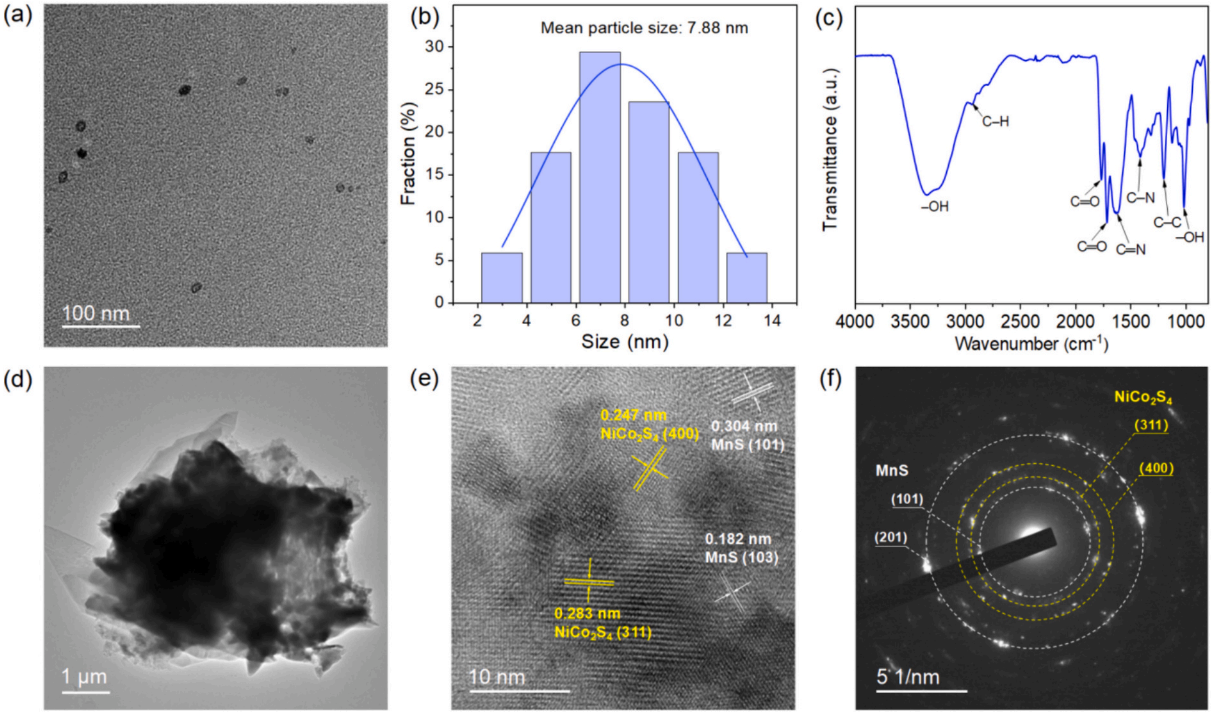

Fig. 4. (a) TME image, (b) size distribution and (c) FTIR spectrum of N-CDs. (d) TME image, (e) high-resolution TEM image, and (f) selected area electron diffraction pattern of Ni-Co-Mn-S@N-CDs sample.

The electrochemical performance of electrode materials was investigated in the three-electrode configuration. Cyclic voltammetry (CV) curves of the Ni-Co-Mn-S@N-CDs electrode at different scan rates are shown in Fig. 5a. The sample exhibits a pair of distinct oxidation and reduction peaks, which is determined by the reversible Faraday redox reaction of Ni^{2+}/Ni^{3+}, Co^{2+}/Co^{3+}, and $Mn^{2+}/Mn^{3+}/Mn^{4+}$ [14]. As the scan rate gradually increases to 30 mV s^{-1}, the oxidation and reduction peaks in the CV curves move to higher and lower voltage, respectively. This is due to the fact that the higher the peak oxidation/reduction current, the higher the energy barrier overcome by the current reaching its peak, and the redox potential will tend to overcome the energy barrier in the direction of high potential voltage and low voltage, respectively. Meanwhile, the closed regions of these CV curves increase substantially, while the shape remains unchanged. The results above suggest that the Ni-Co-Mn-S@N-CDs electrode is electrochemically stable. For reference, Fig. S3a and S3d display CV curves of Ni-Co-Mn-O and Ni-Co-Mn-S electrodes at different scanning rates. In the KOH electrolyte, as the charge storage devices, the redox reactions of the Ni-Co-Mn-S@N-CDs material during charging and discharging could be described as follows [22,35]:

$$NiCo_2S_4 + 4OH^- \leftrightarrow NiSOH + 2CoSOH + SOH^- + 3e^- \quad (6)$$

$$NiSOH + OH^- \leftrightarrow NiSO + H_2O + e^- \quad (7)$$

$$CoSOH + OH^- \leftrightarrow CoSO + H_2O + e^- \quad (8)$$

$$MnS + OH^- \leftrightarrow MnSOH + e^- \quad (9)$$

$$MnSOH + OH^- \leftrightarrow MnSO + H_2O + e^- \quad (10)$$

We use CV curves for electrochemical kinetic studies of electrode materials. The relationship between the peak current (i, mA) and the scanning rates (v, mV s^{-1}) can be described as follows [22]:

$$i = av^b \quad (11)$$

$$logi = loga + blogv \quad (12)$$

where a and b are tunable variables. The electrode sample is classified as battery-type and pseudocapacitive if the value of b is between 0.5 and 1 [23]. In the inset of Fig. 5a, the b value of the Ni-Co-Mn-S@N-CDs electrode is 0.55, which means that the energy storage process of the electrode is diffusion-controlled battery-type and surface-controlled capacitive. In addition, the b values of Ni-Co-Mn-O and Ni-Co-Mn-S samples are shown in Fig. S3b and e in SI. To investigate the reaction mechanism of the Ni-Co-Mn-S@N-CDs electrode, the percentage of the capacitive behavior (k_1v) and the diffusion-controlled behavior ($k_2v^{1/2}$) are calculated from CV curves at a given scanning rate as follows [22]:

$$i = k_1v + k_2v^{1/2} \quad (13)$$

Fig. 5b shows the capacitive behavior ratio and diffusion behavior ratio of the Ni-Co-Mn-S@N-CDs electrode at different scanning rates. The capacitive contribution is as high as 94 % under 30 mV s^{-1}, meaning that the sample shows rapid redox reaction kinetics and superior rate capability. In Fig. 5c, the Ni-Co-Mn-S@N-CDs electrode has the highest redox current density at 5 mV s^{-1}. Moreover, the closed region of the CV curve for the Ni-Co-Mn-S@N-CDs electrode is much larger than those of the Ni-Co-Mn-O and Ni-Co-Mn-S, indicating that the sample has the largest electrochemical capacity. The enhanced performance observed in these results can be attributed to the role of N-CDs in improving the charge transport efficiency of the Ni-Co-Mn-S material. This improvement is a key factor in the material's superior electrochemical behavior. In addition, the closed region of the CV curve for the pure NF is much smaller than those of other electrodes, and the discharge time of the NF at 1 A g^{-1} is very short (Fig. S4), indicating its negligible capacity contribution.

Fig. 5d displays the GCD curves of the Ni-Co-Mn-S@N-CDs sample at different current densities. To compare the capacity of each electrode sample, the GCD curves of the other two electrode samples at different current densities are shown in Fig. S3c and f, respectively. The apparent charge/discharge platforms of the GCD curves in Fig. 5d fully reflect the battery-type energy storage characteristic. The discharge time of the Ni-Co-Mn-S@N-CDs sample is close to the charge time, demonstrating the excellent coulombic efficiency of the electrode. The charge/discharge

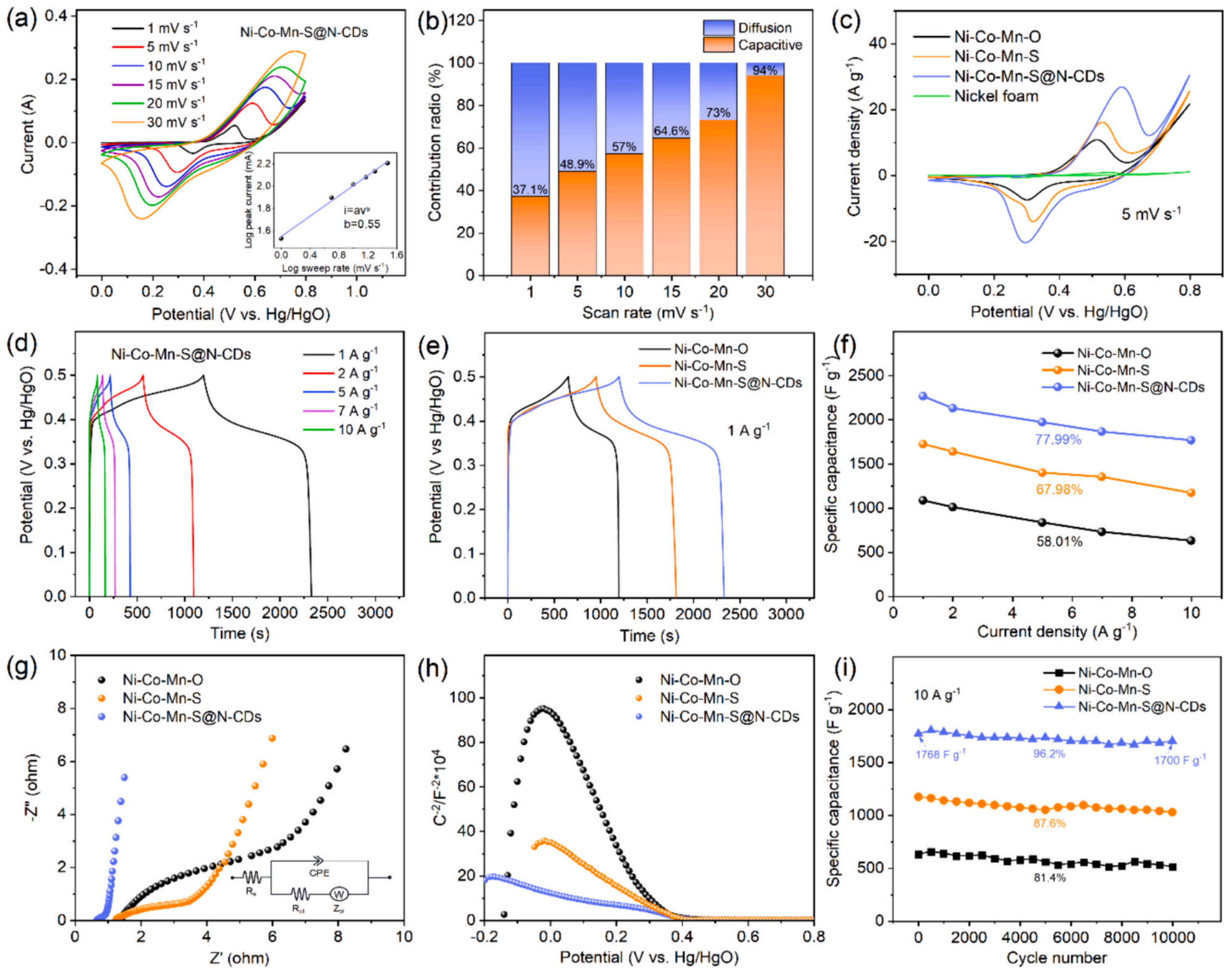

Fig. 5. (a) CV curves of Ni-Co-Mn-S@N-CDs electrode at different scan rates. The inset shows the calculated *b*-value from the relationship between sweep rate and peak current. (b) Contribution ratio of capacitive and diffusion-controlled processes at different scan rates. (c) CV curves of Ni-Co-Mn-O, Ni-Co-Mn-S, Ni-Co-Mn-S@N-CDs, and NF electrodes at the scan rate of 5 mV s^{-1}. (d) GCD curves of Ni-Co-Mn-S@N-CDs electrode at various current densities. (e) GCD curves of Ni-Co-Mn-O, Ni-Co-Mn-S, and Ni-Co-Mn-S@N-CDs electrodes at current density of 1 A g^{-1}. (f) Specific capacitance of Ni-Co-Mn-O, Ni-Co-Mn-S, and Ni-Co-Mn-S@N-CDs electrodes at different current densities. (g) EIS curves and equivalent circuit diagram, and (h) Mott-Schottky curves of Ni-Co-Mn-O, Ni-Co-Mn-S, and Ni-Co-Mn-S@N-CDs electrode materials. (i) Stability performance of Ni-Co-Mn-O, Ni-Co-Mn-S, and Ni-Co-Mn-S@N-CDs electrodes after 10,000 cycles at 10 A g^{-1}.

performance comparison at 1 A g^{-1} for the Ni-Co-Mn-O, Ni-Co-Mn-S, and Ni-Co-Mn-S@N-CDs samples can be found in Fig. 5e. Combined with Table S1, the Ni-Co-Mn-S@N-CDs sample has the highest specific capacity of 2267 F g^{-1} among the three samples, proving that the N-CDs improve the capacitance performance of Ni-Co-Mn-S. In Fig. 5f, the Ni-Co-Mn-S@N-CDs show an impressive capacity retention of 77.99 %, significantly surpassing the performance of the Ni-Co-Mn-O sample and the Ni-Co-Mn-S sample. This superior performance is due to the higher electrical conductivity of Ni-Co-Mn-S than that of Ni-Co-Mn-O and the introduction of highly conductive N-CDs, which effectively increase the charge transfer rate.

Nyquist plots for the three samples are shown in Fig. 5g. We fitted Nyquist plots using Zview software in conjunction with the equivalent circuit diagram (inset of Fig. 5g), and the results are shown in Table S2 in SI. The diameter of the semicircular portion and the intercept with the X-axis of the fitted curve in the high-frequency region are used to represent the charge transfer resistance (R_{ct}) and the equivalent series resistance (R_s), respectively. In the low-frequency region, the slope of the diagonal portion of the fitted curve is used to evaluate the diffusivity of ions through the electrode interface [25]. Compared with the other two electrodes, the R_{ct} of the Ni-Co-Mn-S@N-CDs electrode is as low as 0.33 Ω, indicating that this sample has a remarkable charge transfer rate. Meanwhile, this sample has the lowest R_s of 0.68 Ω, which proves that the N-CDs improve the conductivity of the Ni-Co-Mn-S. In the low-frequency region of the EIS curve, the slope of the Ni-Co-Mn-S@N-CDs sample is highest, suggesting the strongest diffusion capability in the material. This result can be attributed to the fact that the N-CDs shorten the charge transfer path and accelerate the charge transfer rate.

In addition, we analyzed the carrier concentration (N_d) of samples using Mott-Schottky curves (Fig. 5h) based on the following equation for P-type semiconductors [40]:

$$N_d = -(2/e_0\varepsilon\varepsilon_0)\left[\mathrm{d}(1/C^2)/\mathrm{d}V\right]^{-1} \tag{14}$$

where e_0 is the electron charge, ε is the dielectric constant of samples, ε_0 is the dielectric constant of free space, C is the space charge capacitance, and V is the applied bias at the electrode. The Mott-Schottky curves of the three samples demonstrate that these materials all belong to p-type semiconductors. The largest slope of the Mott-Schottky curve for the Ni-Co-Mn-S@N-CDs suggests that Ni-Co-Mn-S@N-CDs has the highest carrier density and electrical conductivity, which is in line with the Nyquist plot results.

The capacitance retention rates of the samples after 10,000 charge/discharge cycles at 10 A g^{-1} are shown in Fig. 5i. The Ni-Co-Mn-S@N-

CDs electrode exhibits the highest capacity retention of 96.2 % among the three samples. The SEM images of the Ni-Co-Mn-S@N-CDs sample before (Fig. S5a and c) and after cycling (Fig. S5b and d) show that the sample retains its rose-like structure, reflecting good structural stability. This result confirms our hypothesis that N-CDs mitigate the volume expansion of Ni-Co-Mn-S and thus improve the cyclic stability. The performance comparison between the Ni-Co-Mn-S@N-CDs and other reported electrode materials is shown in Table S3 in SI. Overall, the Ni-Co-Mn-S@N-CDs electrode exhibits excellent performance in terms of mass capacitance and cyclic stability.

The exceptional electrochemical performance of the Ni-Co-Mn-S@N-CDs electrode material is attributed to these four factors: (1) The rose-like Ni-Co-Mn-S structure provides rich ion transport channels, and the valence transition and synergistic interactions among transition metal ions bring about extensive redox activity, which both improve the reaction kinetics of the electrode material; (2) The N-CDs have abundant hydrophilic functional groups, providing plenty of active sites for the capacity improvement of the electrode material; (3) The excellent electrical conductivity of the N-CDs is beneficial to shorten the charge transfer path, thus enhancing the rate capability of the electrode material; (4) The N-CDs have a prominent electrochemical stability, which can reduce the volume dilatation and strengthen the cycle stability of the electrode material [24,27–29].

To demonstrate the wide applicability of the Ni-Co-Mn-S@N-CDs sample, this positive electrode material is used in a supercapacitor. Fig. 6a shows the schematic of an asymmetric supercapacitor (Ni-Co-Mn-S@N-CDs//AC), where the negative electrode is NF coated with AC, and the solid-state electrolyte is PVA/KOH. The CV curves for AC/NF electrode from 1 mV s^{-1} to 30 mV s^{-1} and the GCD curves from 1 A g^{-1} to 10 A g^{-1} are shown in Fig. S6. This hybrid supercapacitor is used as a power source to feed a load. Fig. 6b exhibits the CV curves for the Ni-Co-Mn-S@N-CDs//AC device at 5 mV s^{-1}, where the effective voltage windows for the device can reach 1.7 V. Fig. 6c presents the CV curves of the device for various voltage windows at 20 mV s^{-1}. Polarization occurs when the voltage rises to 1.8 V, so we used 1.6 V as the stable operating voltage for the device. The CV curves of the Ni-Co-Mn-S@N-CDs//AC supercapacitor at different scanning rates are presented in Fig. 6d. The closed regions of the CV curves increase gradually with the scan rate increasing and the curve shape maintains well, which indicates the rapid reaction rate and the superb electrochemical reversibility of the device.

The GCD curves of the Ni-Co-Mn-S@N-CDs//AC device at different current densities are shown in Fig. 6e. The almost symmetric shape indicates adequate redox reaction and superior coulombic efficiency of the device. The inset of Fig. 6e and Table S4 in SI show that the device has a capacitance of 173.3 F g^{-1} at 1 A g^{-1}, confirming the remarkable capacity of the device. The Ragone plot of the device is shown in Fig. 6f, and the energy densities at different current densities are depicted in the accompanying diagram of Fig. 6f and Table S4 in SI. According to Eqs. (2) and (3), the energy density of the supercapacitor can reach 61.6 Wh kg^{-1} at a power density of 800 W kg^{-1}.

Furthermore, the Ni-Co-Mn-S@N-CDs//AC has an excellent capacity retention rate of 89 % and a terrific coulombic efficiency of 98.63 % after 20,000 cycles at 5 A g^{-1} in Fig. 6g. This is attributed to the fact that the N-CDs with high conductivity and excellent electrochemical stability can shorten the charge transfer path and mitigate the structure destruction during cycling. In the XRD spectrum of Fig. S7, the Ni-Co-

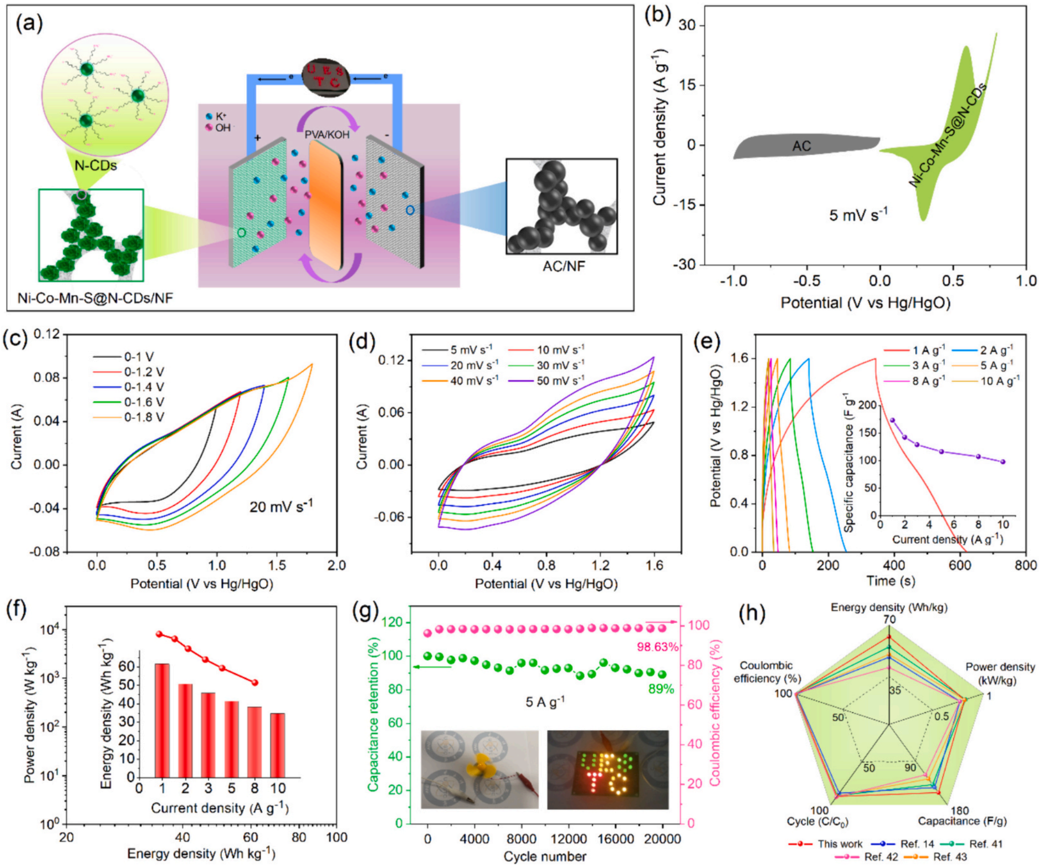

Fig. 6. (a) Schematic diagram of the Ni-Co-Mn-S@N-CDs//AC supercapacitor. (b) CV curves of AC and Ni-Co-Mn-S@N-CDs at the scan rate of 5 mV s^{-1}. (c) CV curves of the device at different potential windows at the scan rate of 20 mV s^{-1}. (d) CV curves of the device at different scan rates ranging from 5 to 50 mV s^{-1}. (e) GCD curves of the device at different current densities. The specific capacitances calculated from GCD curves are shown in the inset. (f) The ragone plot of the device and the inset is the energy densities of the device at different current densities. (g) Cycling performance of the device at 5 A g^{-1} (Inset: a fan powdered by a supercapacitor; LEDs powered by three supercapacitors in series). (h) Electrochemical performance comparison among different supercapacitors.

Mn-S@N-CDs sample after cycling has the same phase composition and crystal planes as the pre-cycling sample. XPS characterizations for the Ni-Co-Mn-S@N-CDs sample after charge/discharge cycle is shown in Fig. S8. The binding energy positions and spin energy differences of all elements are basically unchanged from those of the sample before cycling. These results prove that the Ni-Co-Mn-S@N-CDs sample is chemically stable.

In addition, the Ni-Co-Mn-S@N-CDs//AC supercapacitor demonstrates great adaptability to practical applications. As shown in Fig. S9, the voltage window of two supercapacitors in series is 3.2 V, and the peak current and the charging/discharging time are the same as that of a single device. Additionally, the voltage window of two supercapacitors in parallel is 1.6 V, and the charging/discharging time are twice that of a single device. A fan driven by an electrical motor can be directly powered by one such supercapacitor as shown in the inset of Fig. 6g and Video 1. Moreover, as illustrated in Fig. 6g and Video 2, thirty-six LEDs can be easily illuminated by three supercapacitors in series.

To clearly show the highlights of this work, an electrochemical performance comparison among the Ni-Co-Mn-S@N-CDs//AC with previous works is presented in Fig. 6h. Combined with Table S5, it is apparent that the device has a remarkable electrochemical performance compared with other transition metal compounds, particularly in energy density, specific capacitance, and cycle stability [14,41–43].

The optical images of the Ni-Co-Mn-S@N-CD//AC device after being folded or twisted at different angles are shown in Fig. 7a. The device can function properly under bending, indicating good mechanical stability. Fig. 7b is the CV curves of the device at 20 mV s^{-1} under different bending states. At a maximum folding angle of 180°, the shape of the CV curve is basically unchanged compared with that at 0°; similar results are observed for other deformations. The shape of the GCD curves and the charge/discharge time in Fig. 7c under different bending states remain almost unchanged, and as shown in Fig. 7d, the specific capacity of the device is maintained throughout a bending cycle. These results suggest that the device is flexible enough to withstand real-life operations in wearables and soft robotics.

4. Conclusions

In summary, this research shows the successful synthesis of rose-like Ni-Co-Mn-S materials integrated with N-CDs through a combination of the hydrothermal method and electrodeposition. The obtained Ni-Co-Mn-S@N-CDs electrode material demonstrates exceptional electrochemical properties, including ultrahigh specific capacity of 2276 F g^{-1} at 1 A g^{-1} and superior cycling performance, maintaining 96.2 % of its capacity after 10,000 cycles at 10 A g^{-1}. Moreover, the assembled hybrid supercapacitor using Ni-Co-Mn-S@N-CDs//AC achieves a high energy density of 61.6 Wh kg^{-1} at the power density of 800 W kg^{-1}, along with an outstanding capacitance retention of 89.0 % after 20,000 charge/discharge cycles at 5 A g^{-1}. This work not only marks a significant advance in hybrid solid-state supercapacitors but also highlights their potential for flexible and robust energy storage applications.

Supplementary data to this article can be found online at https://doi.

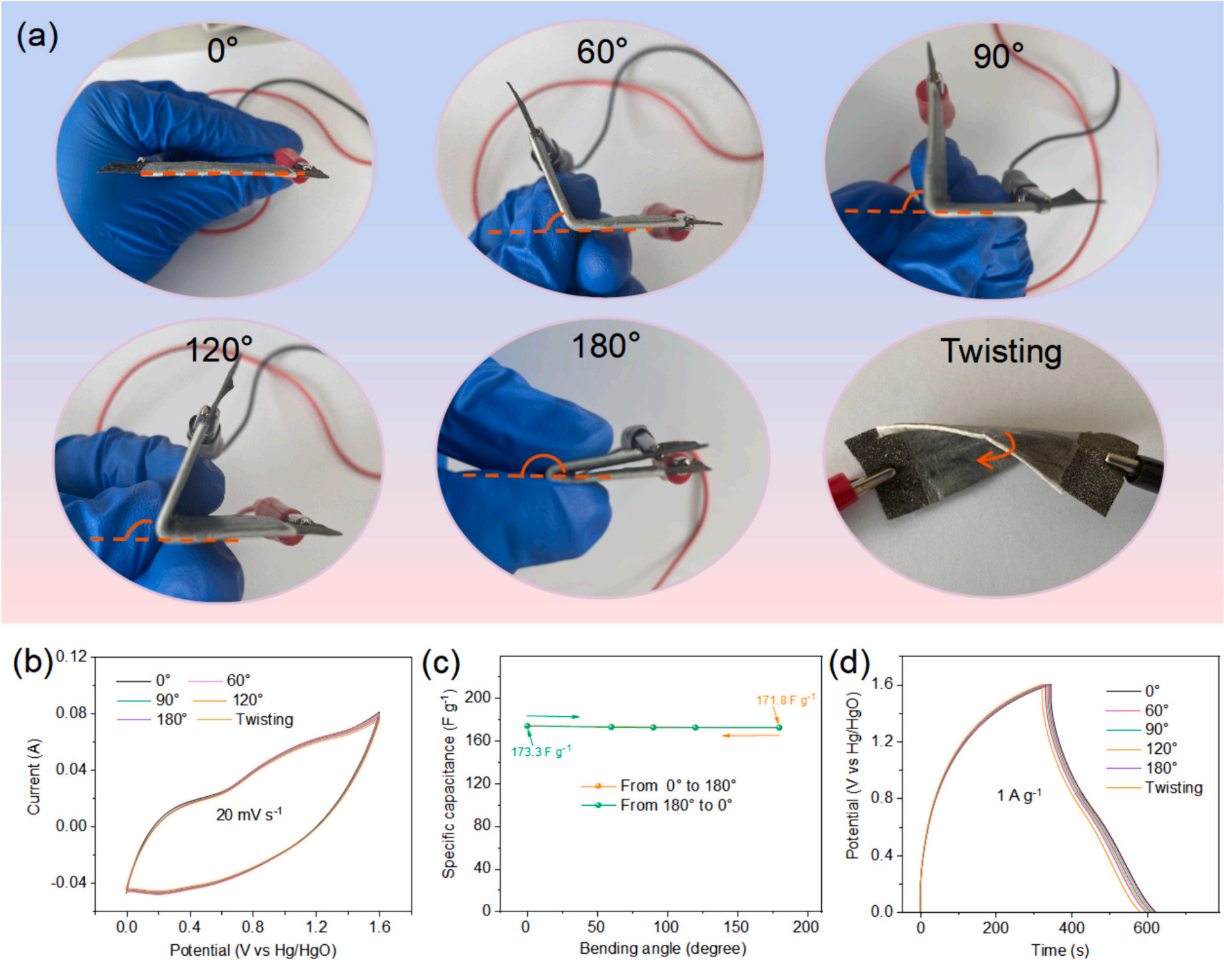

Fig. 7. (a) Optical images of the flexible hybrid supercapacitor Ni-Co-Mn-S@N-CD//AC at different folding and twisting states. (b) CV curves of the device at a scanning rate of 20 mV s^{-1} under various folding conditions. (c) GCD curves of the device at a current density of 1 A g^{-1} under various folding conditions. (d) Specific capacitances of the device under a bending cycle.

org/10.1016/j.est.2024.112039.

CRediT authorship contribution statement

Bin Lu: Writing – review & editing, Writing – original draft, Visualization, Methodology, Investigation, Data curation. **Guo-Tao Xiang:** Software, Methodology, Investigation, Formal analysis, Conceptualization. **Jia-Lei Xu:** Visualization, Investigation. **Rui-Dong Shi:** Software, Formal analysis. **Na Chen:** Supervision, Investigation. **Yong-Da Hu:** Supervision, Resources. **Raul D. Rodriguez:** Writing – review & editing, Supervision. **Jin-Ju Chen:** Writing – review & editing, Validation, Supervision, Resources, Conceptualization.

Declaration of competing interest

There are no conflicts of interest to declare.

Data availability

Data will be made available on request.

Acknowledgements

This work was supported by Sichuan Science and Technology Program (grant No. 2023YFG0215) and Chengdu Science and Technology Program (grant No. 2023-GH02-00021-HZ).

References

[1] K. Poonam, A. Arora Sharma, S.K. Tripathi, Review of supercapacitors: materials and devices, J. Energy Storage 21 (2019) 801–825, https://doi.org/10.1016/j.est.2019.01.010.

[2] P. Lamba, P. Singh, P. Singh, P. Singh, Bharti, A. Kumar, M. Gupta, Y. Kumar, Recent advancements in supercapacitors based on different electrode materials: classifications, synthesis methods and comparative performance, J. Energy Storage 48 (2022) 103871, https://doi.org/10.1016/j.est.2021.103871.

[3] B. Xu, H.B. Zhang, H. Mei, D.F. Sun, Recent progress in metal-organic framework-based supercapacitor electrode materials, Coord. Chem. Rev. 420 (2020) 213438, https://doi.org/10.1016/j.ccr.2020.213438.

[4] C.Z. Wei, R. Zhang, X. Zheng, Q.L. Ru, Q.Y. Chen, C. Cui, G. Li, D.J. Zhang, Hierarchical porous $NiCo_2O_4/CeO_2$ hybrid materials for high performance supercapacitors, Inorg. Chem. Front. 5 (2018) 3126–3134, https://doi.org/10.1039/C8QI01010B.

[5] C.Z. Wei, J. Sun, Y.C. Zhang, Y. Liu, Z.C. Guo, W.M. Du, L. Liu, Y.M. Zhang, Hierarchical $Ni(OH)_2$-MnO_2 hollow spheres as an electrode material for high-performance supercapacitors, Inorg. Chem. Front. 9 (2022) 3542–3551, https://doi.org/10.1039/D2QI00780K.

[6] T.T. Yu, S.B. Li, F.B. Li, L. Zhang, Y.P. Wang, J.Y. Sun, In-situ synthesized and induced vertical growth of cobalt vanadium layered double hydroxide on few-layered V_2CT_x MXene for high energy density supercapacitors, J. Colloid Interface Sci. 661 (2024) 460–471, https://doi.org/10.1016/j.jcis.2024.01.206.

[7] B.R. Lu, S.B. Li, J. Pan, L. Zhang, J.J. Xin, Y. Chen, X.G. Tan, pH-controlled assembly of five new organophosphorus strandberg-type cluster-based coordination polymers for enhanced electrochemical capacitor performance, Inorg. Chem. 59 (2020) 1702–1714, https://doi.org/10.1021/acs.inorgchem.9b02858.

[8] J. Pan, S.B. Li, L. Zhang, T.T. Yu, F.B. Li, W.Z. Zhang, J.X. Wang, D.Q. Zhang, Y. Yu, X. Li, Reduced graphene oxide/Ni foam supported ZIF-67 derived $CuCo_2S_4$@CoS_2 core-shell heterostructure for boosted electrochemical energy storage, J. Energy Storage 47 (2022) 103550, https://doi.org/10.1016/j.est.2021.103550.

[9] P.B. Geng, S.S. Zheng, H. Tang, R.M. Zhu, L. Zhang, S. Cao, H.G. Xue, H. Pang, Transition metal sulfides based on graphene for electrochemical energy storage, Adv. Energy Mater. 8 (2018) 1703259, https://doi.org/10.1002/aenm.201703259.

[10] C.Z. Wei, Q.Y. Chen, C. Chen, R. Liu, Q. Zhang, L.P. Zhang, Mesoporous nickel cobalt manganese sulfide yolk-shell hollow spheres for high-performance electrochemical energy storage, Inorg. Chem. Front. 6 (2019) 1851–1860, https://doi.org/10.1039/C9QI00173E.

[11] M.I.A. Abdel Maksoud, R.A. Fahim, A.E. Shalan, M. Abd Elkodous, S.O. Olojede, A. I. Osman, C. Farrell, A.H. Al-Muhtaseb, A.S. Awed, A.H. Ashour, D.W. Rooney, Advanced materials and technologies for supercapacitors used in energy conversion and storage: a review, Environ. Chem. Lett. (19) (2021) 375–439, https://doi.org/10.1007/s10311-020-01075-w.

[12] C.X. Kang, L. Ma, Y.C. Chen, L.K. Fu, Q. Hu, C.B. Zhou, Q.M. Liu, Metal-organic framework derived hollow rod-like NiCoMn ternary metal sulfide for high-performance asymmetric supercapacitors, Chem. Eng. J. 427 (2022) 131003, https://doi.org/10.1016/j.cej.2021.131003.

[13] H.B. Wang, W.F. Cai, L.Q. He, M.L. Zhu, Y. Wang, Anchoring ternary NiCoMn-S ultrathin nanosheets on porous $ZnCo_2O_4$ nanowires to form core-shell composites for high-performance asymmetric supercapacitor, J. Alloys Compd. 870 (2021) 159347, https://doi.org/10.1016/j.jallcom.2021.159347.

[14] W. Yan, H.Y. Zeng, K. Zhang, Y.W. Long, M.X. Wang, Ni-Co-Mn hydrotalcite-derived hierarchically porous sulfide for hybrid supercapacitors, J. Colloid Interface Sci. 635 (2023) 379–390, https://doi.org/10.1016/j.jcis.2022.12.144.

[15] R.Q. Liu, S.S. Xu, X.X. Shao, Y. Wen, X.R. Shi, L.P. Huang, M. Hong, J. Hu, Z. Yang, Defect-engineered NiCo-S composite as a bifunctional electrode for high-performance supercapacitor and electrocatalysis, ACS Appl. Mater. Interfaces 13 (2021) 47717–47727, https://doi.org/10.1021/acsami.1c15824.

[16] X. Wang, L. Tian, X. Long, M.Z. Yang, X.Q. Song, W.L. Xie, D.Q. Liu, Y.J. Fu, J.S. Li, Y.L. Li, Cracked bark-inspired ternary metallic sulfide ($NiCoMnS_4$) nanostructure on carbon cloth for high-performance aqueous asymmetric supercapacitors, Sci. China Mater. 64 (2021) 1632–1641, https://doi.org/10.1007/s40843-020-1562-1.

[17] G.T. Fu, J.M. Lee, Ternary metal sulfides for electrocatalytic energy conversion, J. Mater. Chem. A 7 (2019) 9386, https://doi.org/10.1039/C9TA01438A.

[18] A. Alam, G. Saeed, K.-H. Kim, S. Lim, Metal-organic framework-derived NiS@Cobalt-Molybdenum layered double hydroxides shell@core as cathode and $CoFe_2O_4$-nanoparticles@MXene shell@core as anode materials for ultra-high energy-density flexible asymmetric supercapacitor, J. Energy Storage 55 (2022) 105592, https://doi.org/10.1016/j.est.2022.105592.

[19] K.P. Shwetha, C. Manjunatha, M.K. Sudha Kamath, C.K. Rastogi, V. Chaudhary, G. Maurya, Y. Athreya, B.W. Shivaraj, A. Khosla, Fabrication of super-high energy density asymmetric supercapacitor prototype device employing $NiCo_2S_4$@f-MWCNT nanocomposite, J. Energy Storage 72 (2023) 108657, https://doi.org/10.1016/j.est.2023.108657.

[20] B.F. Tao, W.S. Yang, M. Zhou, L.R. Qiu, S.S. Lu, X.H. Wang, Q. Zhao, Q. Xie, Y. J. Ruan, Designing a carbon nanofiber-encapsulated iron carbide anode and nickel-cobalt sulfide-decorated carbon nanofiber cathode for high-performance supercapacitors, J. Colloid Interface Sci. 621 (2022) 139–148, https://doi.org/10.1016/j.jcis.2022.04.076.

[21] Z.W. Lu, Y. Zhang, M.M. Sun, P. Zou, X.X. Wang, Y.Y. Wang, Q.M. Huang, H. P. Chen, J.S. Ye, H.B. Rao, N-doped carbon dots regulate porous hollow nickel-cobalt sulfide: high-performance electrode materials in supercapacitor and enzymeless glucose sensor, J. Power Sources 516 (2021) 230685, https://doi.org/10.1016/j.jpowsour.2021.230685.

[22] Z.Y. Zhang, J. Wang, Z.Y. Zhu, X. Ma, K.J. Fang, C. Wang, L.X. Kang, Z.H. Pan, G. D. Nie, Scalable in-situ formation of amorphous $NiCoS_x$ nanosheets on porous carbon-based nanofibers for asymmetric supercapacitors, Sci. China-Mater. 66 (2023) 3484–3492, https://doi.org/10.1007/s40843-023-2513-0.

[23] X.N. Li, W.Y. Zhang, H.W. Kang, H.L. Liu, B.C. Yang, Z.J. Li, Z.K. Li, Self-assembled $CoS_2/NiCo_2S_4$/RGO nanohybrids as advanced electrode for hybrid supercapacitor with enhanced energy density and ultra-long durability, J. Energy Storage 67 (2023) 107528, https://doi.org/10.1016/j.est.2023.107528.

[24] F.A. Permatasari, M.A. Irham, S.Z. Bisri, F. Iskandar, Carbon-based quantum dots for supercapacitors: recent advances and future challenges, Nanomaterials 11 (1) (2021) 91, https://doi.org/10.3390/nano11010091.

[25] V. Gayathri, E. Praveen, K. Jayakumar, S. Karazhanov, C.R. Mohan, Graphene quantum dots assisted $CuCo_2S_4$/MWCNT nanoflakes as superior bifunctional electrocatalysts for dye-sensitized solar cell and supercapacitor applications, Colloids Surf. A Physicochem. Eng. Asp. 662 (2023) 130948, https://doi.org/10.1016/j.colsurfa.2023.130948.

[26] K.Q. Qu, M.H. Chen, W.C. Wang, S. Yang, S.J. Jing, S.T. Guo, J.Y. Tian, H.J. Qi, Z. H. Huang, Biomass-derived carbon dots regulating nickel cobalt layered double hydroxide from 2D nanosheets to 3D flower-like spheres as electrodes for enhanced asymmetric supercapacitors, J. Colloid Interface Sci. 616 (2022) 584–594, https://doi.org/10.1016/j.jcis.2022.02.110.

[27] C.K. Maity, S. De, A. Panigrahi, S. Acharya, K. Verma, M.J. Kim, G.C. Nayak, Aerosol derived carbon dots decorated boron nitride supported Zn-doped MoS_2 for high performing flexible asymmetric supercapacitor, Compos. Part B Eng. 264 (2023) 110887, https://doi.org/10.1016/j.compositesb.2023.110887.

[28] S. Yetiman, H. Peçenek, F.K. Dokan, M.S. Onses, E. Yilmaz, E. Sahmetlioglu, Microwave-assisted fabrication of high-performance supercapacitors based on electrodes composed of cobalt oxide decorated with reduced graphene oxide and carbon dots, J. Energy Storage 49 (2022) 104103, https://doi.org/10.1016/j.est.2022.104103.

[29] J.M. Wang, Z.B. Fang, T. Li, S.U. Rehman, Q.H. Luo, P. Chen, L. Hu, F.P. Zhang, Q. Y. Wang, H. Bi, Highly hydrophilic carbon dots' decoration on $NiCo_2O_4$ nanowires for greatly increased electric conductivity, supercapacitance, and energy density, Adv. Mater. Interfaces 6 (9) (2019) 1900049, https://doi.org/10.1002/admi.201900049.

[30] Y. Liang, Y.M. Liu, S.Y. Li, B. Lu, C.L. Liu, H.J. Yang, X.Y. Ren, Y.L. Hou, Hydrothermal growth of nitrogen-rich carbon dots as a precise multifunctional probe for both Fe^{3+} detection and cellular bio-imaging, Opt. Mater. 89 (2019) 92–99, https://doi.org/10.1016/j.optmat.2019.01.008.

[31] Y.C. Li, J.C. Liu, T.L. Gong, C.Z. Liang, L. Li, X.M. Lin, Z.R. Ying, H.Y. Liu, One-step hydrothermal preparation of a novel 2D MXene-based composite electrode material synergistically modified by CuS and carbon dots for supercapacitors, J. Alloys Compd. 947 (2023) 169400, https://doi.org/10.1016/j.jallcom.2023.169400.

[32] Y. Zhang, L.J. Huang, X.X. Lei, H. Huang, W. Guo, S. Wang, Hierarchical ternary Zn-Ni-Co sulfide/oxide heterostructure for high specific energy hybrid supercapacitor, J. Alloys Compd. 962 (2023) 171201, https://doi.org/10.1016/j.jallcom.2023.171201.

[33] J.H. Cao, Y.Z. Hua, Y.Y. Zhu, H.J. Cao, M.Q. Fan, C.H. Huang, K.Y. Shu, M.X. He, H. C. Chen, Synthesis of mesoporous nickel-cobalt-manganese sulfides as electroactive materials for hybrid supercapacitors, Chem. Eng. J. 405 (2021) 126928, https://doi.org/10.1016/j.cej.2020.126928.

[34] H.P. Zhang, Y.Q. Xie, S. Yang, X. Gao, H. Bai, F. Yao, H.Y. Yue, $NiCo_2S_4$ nanocone arrays on three-dimensional graphene with small hole diameters for asymmetric supercapacitor, J. Alloys Compd. 968 (2023) 171694, https://doi.org/10.1016/j.jallcom.2023.171694.

[35] M. Yang, H.H. Ning, L. Xiao, F.H. Cui, F.C. Zhang, Mn_3O_4/MnS heterostructure for electrode and asymmetric supercapacitor under high charge/discharge current, Electrochim. Acta 424 (2022) 140630, https://doi.org/10.1016/j.electacta.2022.140630.

[36] Y. Wang, F. Xu, L.X. Sun, S.W. Fang, J.H. Lao, C.C. Zhang, S.Y. Wei, L.M. Liao, Y. X. Guan, Y.P. Xia, Y.M. Luo, Y.J. Sun, Y.J. Zou, Z.Z. Yu, Q.W. Shao, Y.L. Zhu, Y. Luo, Controllable preparation of nickel cobalt manganese ternary metal-organic frameworks for high-performance supercapacitor, J. Energy Storage 58 (2023) 106395, https://doi.org/10.1016/j.est.2022.106395.

[37] E. Dhandapani, N. Duraisamy, R. Rajedran, Carbon-quantum-dots-anchored poly (aniline-co-indole) composite electrodes for high-performance supercapacitor applications, ACS Appl. Polym. Mater. 5 (2023) 7420–7432, https://doi.org/10.1021/acsapm.3c01237.

[38] P.W. Gong, L. Sun, F. Wang, X.C. Liu, Z.Q. Yan, M.Z. Wang, L. Zhang, Z.Z. Tian, Z. Liu, J.M. You, Highly fluorescent N-doped carbon dots with two-photon emission for ultrasensitive detection of tumor marker and visual monitor anticancer drug loading and delivery, Chem. Eng. J. 356 (2019) 994–1002, https://doi.org/10.1016/j.cej.2018.09.100.

[39] L. Jiang, H.H. Ding, M.S. Xu, X.L. Hu, S.L. Li, M.Z. Zhang, Q. Zhang, Q.Y. Wang, S. Y. Lu, Y.P. Tian, H. Bi, UV–Vis–NIR full-range responsive carbon dots with large multiphoton absorption cross sections and deep-red fluorescence at nucleoli and in vivo, Small 16 (2020) 2000680, https://doi.org/10.1002/smll.202000680.

[40] D. Xiong, Q. Zhang, S.K. Verma, X.Q. Bao, H. Li, X.J. Zhao, Crystal structural, optical properties and mott-schottky plots of p-type Ca doped $CuFeO_2$ nanoplates, Mater. Res. Bull. 83 (2016) 141–147, https://doi.org/10.1016/j.materresbull.2016.05.031.

[41] X.H. Tang, Y.H. Lui, B.W. Zhang, S. Hu, Venus flytrap-like hierarchical NiCoMn-O@$NiMoO_4$@C nanosheet arrays as free-standing core-shell electrode material for hybrid supercapacitor with high electrochemical performance, J. Power Sources 477 (2020) 228977, https://doi.org/10.1016/j.jpowsour.2020.228977.

[42] Y.F. Cheng, K.D. Xia, H.B. Li, P.F. Liu, Z.F. Zhao, G.R. Xu, F. Wahid, H.J. Wang, One-pot synthesis of NiO-$MnCo_2O_4$ heterostructure hollow spheres via template-free solvothermal method for high-performance supercapacitors, Colloids Surf. A Physicochem. Eng. Asp. 669 (2023) 131544, https://doi.org/10.1016/j.colsurfa.2023.131544.

[43] C.Y. Deng, J.H. He, G.J. Wang, K. Wang, W. Dong, X.D. Hong, Cyclic voltammetry activation for boosting the supercapacitance of trimetallic Ni-Co-Mn phosphides, Appl. Surf. Sci. 616 (2023) 156526, https://doi.org/10.1016/j.apsusc.2023.156526.